JOURNAL OF THE AMERICAN CHEMICAL SOCIETY

pubs.acs.org/JACS

Article

What is the Real Origin of the Activity of Fe−N−C Electrocatalysts in the O_2 Reduction Reaction? Critical Roles of Coordinating Pyrrolic N and Axially Adsorbing Species

Xu Hu, Suya Chen, Letian Chen, Yun Tian, Sai Yao, Zhengyu Lu, Xu Zhang,* and Zhen Zhou*

Cite This: *J. Am. Chem. Soc.* 2022, 144, 18144−18152

Read Online

ACCESS | Metrics & More | Article Recommendations | Supporting Information

ABSTRACT: Fe−N−C electrocatalysts have emerged as promising substitutes for Pt-based catalysts for the oxygen reduction reaction (ORR). However, their real catalytic active site is still under debate. The underlying roles of different types of coordinating N including pyridinic and pyrrolic N in catalytic performance require thorough clarification. In addition, how to understand the pH-dependent activity of Fe−N−C catalysts is another urgent issue. Herein, we comprehensively studied 13 different N-coordinated FeN_xC configurations and their corresponding ORR activity through simulations which mimic the realistic electrocatalytic environment on the basis of constant-potential implicit solvent models. We demonstrate that coordinating pyrrolic N contributes to a higher activity than pyridinic N, and pyrrolic FeN_4C exhibits the highest activity in acidic media. Meanwhile, the *in situ* active site transformation to $^*O$-FeN_4C and $^*OH$-FeN_4C clarifies the origin of the higher activity of Fe−N−C in alkaline media. These findings can provide indispensable guidelines for rational design of better durable Fe−N−C catalysts.

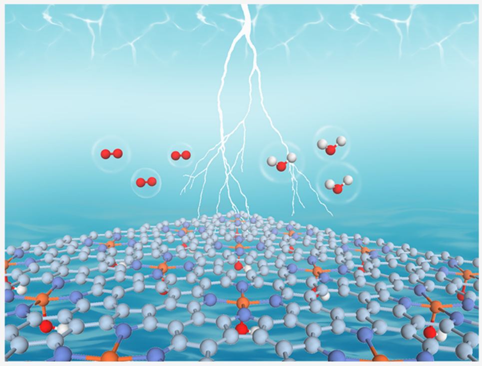

INTRODUCTION

Understanding the electrocatalytic mechanism of the oxygen reduction reaction (ORR) is the fundamental prerequisite for the further development of proton-exchange membrane fuel cells (PEMFCs) and metal−air batteries, which are the most promising strategies for sustainable energy utilization and transport electrification. However, the sluggish reaction dynamics inherent in the ORR process generally requires scarce and expensive Pt-based catalysts. In recent years, metal−nitrogen-codoped carbon matrix (M−N−C) single-atom catalysts (SACs) have emerged as a comparable alternative to Pt-based catalysts; especially, FeN_xC SACs outperform other M−N−C SACs.[1−4]

Unveiling the intrinsic catalytic active sites of FeN_xC SACs is the foundation for improving their catalytic activity and long-term stability. The synthesis of SACs poses a formidable challenge for experimental scientists to clarify which coordination environment makes a significant contribution to the superior catalytic activity of FeN_xC SACs, where first-principles computations could help resolve the myth. Generally, there are two types of coordinating N atoms, pyridinic and pyrrolic N, in FeN_xC SACs. Most current experiments ascribed the pyridinic-type FeN_4 as the catalytic active site. Zhang et al.[5] synthesized Fe SAC-MOF-5 catalysts with high ORR activity in 0.5 M H_2SO_4, and the active site was determined to be pyridinic FeN_4. Jiang et al.[6] prepared pyridinic-type single-atom FeN_4C catalysts through pyrolysis of SiO_2@MOF composites with good performance in both alkaline and acidic media. However, controversy arises since some other experimental reports attributed the high activity to pyrrolic N. Xie et al.[7] successfully developed a high-purity pyrrole-type FeN_4 ORR catalyst that revealed significantly enhanced activity compared with a pyridinic-type one through NH_3 pyrolysis. Cao et al.[8] proposed a surfactant-assisted method to synthesize Fe SACs and determined that Fe-pyrrolic-N is the origin of high ORR activity. Even though X-ray photoelectron spectroscopy (XPS) has been widely used to determine both N types in experiments, including pyridinic and pyrrolic N,[9,10] the current computations often consider only one type of N due to its dominance in XPS, which would potentially result in a large gap between experiments and computations, especially when the activity of the two types of N differs a lot. Therefore, it is still ambiguous as to which type of coordinating N of FeN_xC is the most relevant active site for ORR from both experimental and computational perspectives, which is imperative for us to explore.

The computational hydrogen electrode (CHE) model has been extensively applied in electrocatalytic simulations and made huge success in explaining reaction mechanisms and

Received: August 17, 2022
Published: September 22, 2022

predicting promising catalysts for ORR despite its great simplicity.[11,12] However, this model could not accurately reflect the adsorption energy as the configuration of reaction intermediates is dependent on the applied electrode potential. Thus, the free energy profile referenced to the reversible hydrogen electrode (RHE) scale could not reflect the pH dependence with the CHE model due to the cancellation of pH and electrode potential corrections. Though many experiments illustrated that the ORR activity for FeN_xC SACs was higher in alkaline than in acidic media,[13,14] the pH-dependent activity is still a critical issue, which cannot be reflected by the computations on the CHE model. To resolve this problem, electrocatalytic simulations under a more realistic environment by taking both solvent and constant-potential effects into consideration are essential to acquire a reliable atomic understanding of reaction mechanisms.[15,16]

Here, we adopted the double-reference method[17,18] combined with the implicit solvent model to simulate the energetics of ORR catalyzed by FeN_xC SACs to elucidate the intrinsic catalytic active site and pH-dependent activity.[19]

■ COMPUTATIONAL METHODS

The Vienna Ab initio simulation package (VASP) was used to perform all of the spin-polarized density functional theory (DFT) computations.[20] The Perdew−Burke−Ernzerhof (PBE) functional within the generalized gradient approximation (GGA) was used to describe the exchange−correlation interaction.[21] In static computations and structure optimization, the cutoff energy of the plane wave basis set was set to 400 eV. We used a model of a pristine graphene layer with 32 and 26 C atoms and removed two C atoms to anchor the Fe atom and replaced the surrounding four C atoms with x (x = 1−4) nitrogen atoms to simulate the pyrrole-type and pyridinic-type FeN_xC SACs. A vacuum layer of 15 Å was used to prevent the interaction between periodic images. The zero damping DFT-D3 method of Grimme was used to consider the vdW corrections. The γ-centered Monkhorst−Pack scheme with a K-point resolved value of 0.08 π/Å was used in all DFT computations.[22] The ionic relaxation step was breached when the norms of all of the forces were smaller than 0.05 eV/Å. The VASPKIT code was used for postprocessing of the VASP computational data.[23]

We adopted the double-reference method to simulate the energetics of ORR catalyzed by FeN_xC SACs to elucidate the intrinsic catalytic active sites under reaction conditions and the pH-dependent activity.[19] The solvent environment was modeled by the VASPsol code.[24,25] The relative permittivity was set to 80 to model the aqueous electrolyte. The effective surface tension parameter was assigned to 0 in VASPsol to neglect the cavitation energy contribution. The linearized Poisson−Boltzmann model with a Debye length of 3.0 Å mimics the compensating charge. To clarify the reaction mechanism under different electrode potentials, we varied the excess charge of the unit cell (Δn) from −2.0 e to +2.0 e in steps of 0.5 e. Figure 1 shows an example of the coupling between the applied potential and adsorption configuration and the corresponding ion distribution.

The potential-dependent energy of the system (E) is defined in eq 1.

$$E = E_{DFT} - \Delta n(V_{sol} + \Phi_q/e) \quad (1)$$

where E_{DFT} is the DFT-calculated energy, V_{sol} is the electrostatic potential of the bulk electrolyte, and $-\Phi_q$ is the work function of the charged system. The relation between Φ_q and the corresponding electrode potential referenced to the standard hydrogen electrode (SHE) scale is formulated in eq 2.

$$U_q(\text{V/SHE}) = -4.6\ \text{V} - \Phi_q/e \quad (2)$$

where −4.6 V is the absolute electrode potential of the SHE benchmarked in VASPsol.

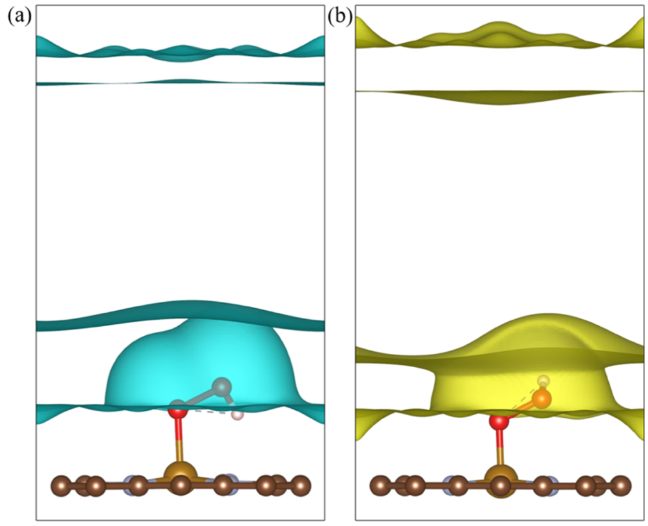

Figure 1. Ionic countercharge density iso-surfaces of 1×10^{-6} e/Å^{-3} for *OOH adsorbed on pyrrolic FeN_4C corresponding to (a) −2.01 V/SHE and (b) 1.88 V/SHE, adjusted by adding and removing two electrons, respectively. The cyan and yellow areas indicate positively and negatively charged ions, respectively. C, brown; N, grayish blue; O, red; H, pink; and Fe, gold.

The $E-U_q$ points follow a quadratic function as

$$E(U_q) = -\frac{1}{2}C(U_q - U_0)^2 + E_0 \quad (3)$$

where U_0, C, and E_0 are the fitted values of the potential of zero charge (PZC), capacitance of the corresponding system, and the energy of the system at the PZC, respectively.

The 4e$^-$ ORR mechanism in acidic media is listed as follows

$$O_2 + H^+ + e^- + * \rightarrow *OOH \quad (4)$$

$$*OOH + H^+ + e^- \rightarrow *O + H_2O \quad (5)$$

$$*O + H^+ + e^- \rightarrow *OH \quad (6)$$

$$*OH + H^+ + e^- \rightarrow * + H_2O \quad (7)$$

Note that the free energy change of each elementary step is the same in alkaline media due to $G(H^+) + G(OH^-) = G(H_2O)$ under thermodynamic equilibrium conditions. The free energy change of each elementary step is calculated as $\Delta G = \Delta E + T\Delta S + \Delta ZPE$, where ΔE is the potential-dependent energy and $T\Delta S$ and ΔZPE are the entropy change and zero-point energy change, respectively. The free energies of O_2, H_2O, and H_2 are listed in Table S1. The equilibrium potential for 4e$^-$ and 2e$^-$ ORR are 1.23 and 0.68 V/SHE, respectively.

The adsorption energies of three reaction intermediates (*OOH, *O, and *OH) in ORR are calculated as follows

$$E_{ads}(*OOH) = E(*OOH) - E(\text{slab}) - 2E(H_2O) + \frac{3}{2}E(H_2) \quad (8)$$

$$E_{ads}(*O) = E(*O) - E(\text{slab}) - E(H_2O) + E(H_2) \quad (9)$$

$$E_{ads}(*OH) = E(*OH) - E(\text{slab}) - E(H_2O) + \frac{1}{2}E(H_2) \quad (10)$$

To determine the thermodynamically favorable active site of FeN_xC SACs under reaction conditions and evaluate the acidic stability against metal dissolution, we employed the model proposed by Holby et al.[26] The detailed metal dissolution and active site transformation under different reaction conditions are listed as follows

$$FeN_yC + nH^+ \rightarrow Fe^{2+} + N_yCH_n + (2 - n)e^- \quad (11)$$

https://doi.org/10.1021/jacs.2c08743
J. Am. Chem. Soc. 2022, 144, 18144−18152

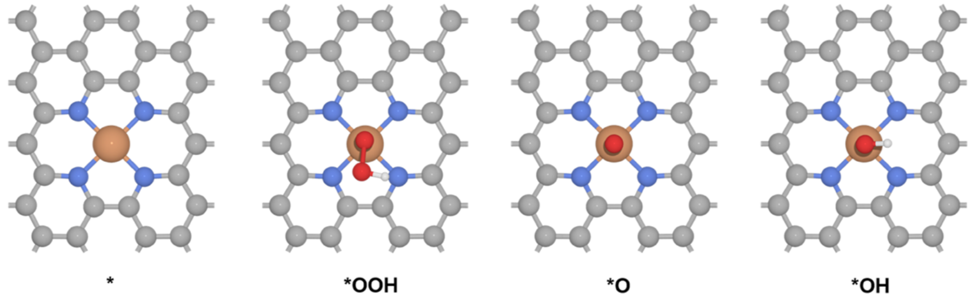

Figure 2. Optimized reaction models during ORR catalyzed by pyridinic FeN_4C at zero excess charges, pyridinic FeN_4C slab, *OOH, *O, and *OH. C, gray; N, blue; O, red; H, white; and Fe, brown.

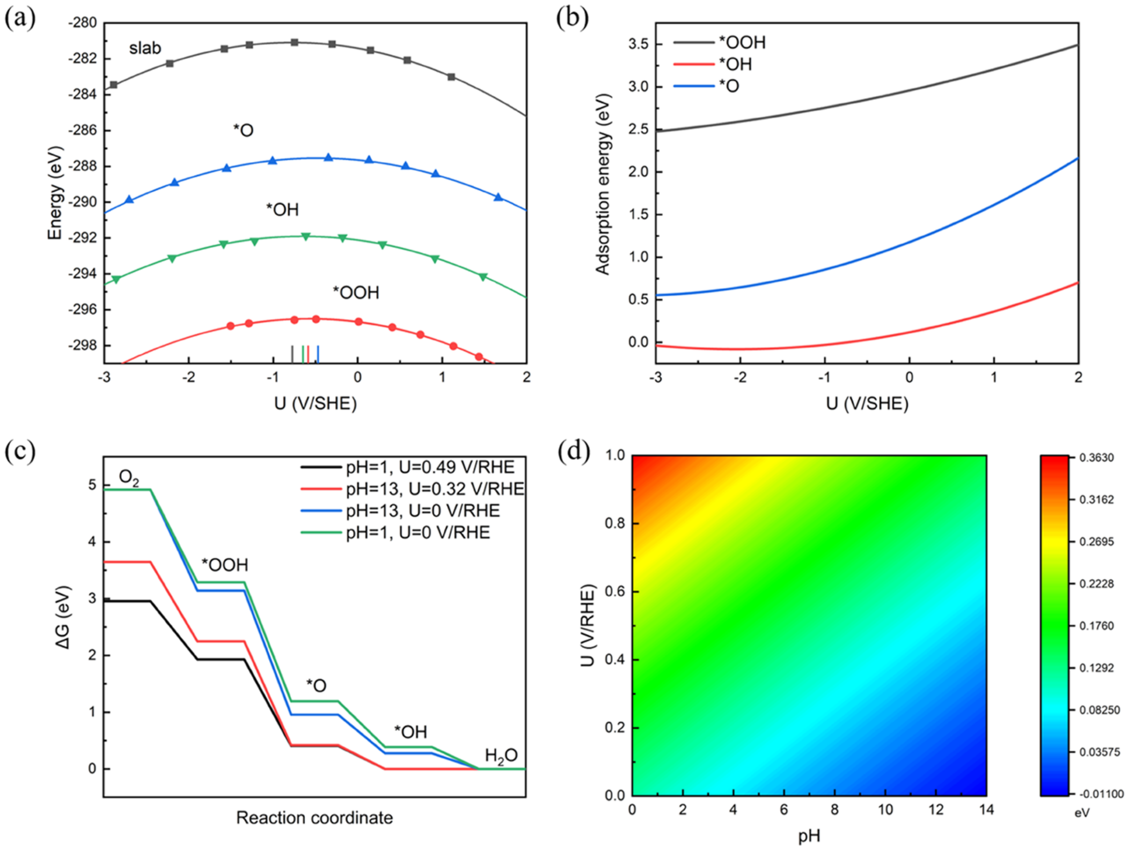

Figure 3. (a) Calculated energies of the bare pyridinic FeN_4C slab (black) and corresponding three reaction intermediates (*OOH, red; *O, blue; *OH, green) as a function of the applied electrode potential. (b) Adsorption energies of *OOH, *O, and *OH as a function of the applied electrode potential. (c) Free energy profile of ORR catalyzed by pyridinic FeN_4C at U = 0.49 V/RHE, pH = 1; U = 0.32 V/RHE, pH = 13; U = 0 V/RHE, pH = 13; and U = 0 V/RHE, pH = 1. (d) pH-dependent and potential-dependent contour plot of adsorption energies of *OH on pyridinic FeN_4C.

$$FeN_yC + nH^+ \rightarrow Fe^{3+} + N_yCH_n + (3 - n)e^- \quad (12)$$

$$FeN_yC + (n - 1)H^+ + H_2O \rightarrow FeOH^{2+} + N_yCH_n + (3 - n)e^- \quad (13)$$

$$FeN_yC + H_2O \rightarrow {}^*O{-}FeN_yC + 2H^+ + 2e^- \quad (14)$$

$$FeN_yC + H_2O \rightarrow {}^*OH{-}FeN_yC + H^+ + e^- \quad (15)$$

where N_yCH_n is the catalytic active site after metal dissolution, and we anticipated that the remaining N groups would be protonated readily based on the protonation free energy change and previous reports.[27,28] Fe^{2+}, Fe^{3+}, and $FeOH^{2+}$ are the dissolved metal ions, and the ion concentration is assumed to be 10^{-6} M to get a qualitative trend as done in the previous reports.[27,29] Since oxygen and hydroxyl may be exchanged between the catalyst surface and the water solvent, *O-FeN_yC and *OH-FeN_yC are determined to be active sites bonding with axial O and OH under corresponding working conditions, respectively, which has been reported experimentally and computationally.[26,27,30]

■ RESULTS AND DISCUSSION

Based on experimental and computational studies,[7,8,31−33] we constructed 13 different N-coordinated FeN_xC configurations, as shown in Figures S1, S2, and 2.

First, we studied the pyridinic FeN_4C, which has been extensively studied in many experiments and computations based on the CHE model, without considering the applied potential and solvent effect. Here, we investigated the reaction

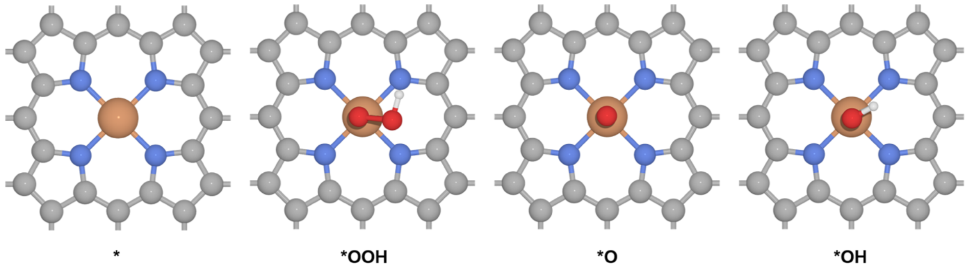

Figure 4. Optimized reaction models during the ORR catalyzed by pyrrolic FeN_4C at zero excess charges, pyrrolic FeN_4C slab, *OOH, *O, and *OH. C, gray; N, blue; O, red; H, white; and Fe, brown.

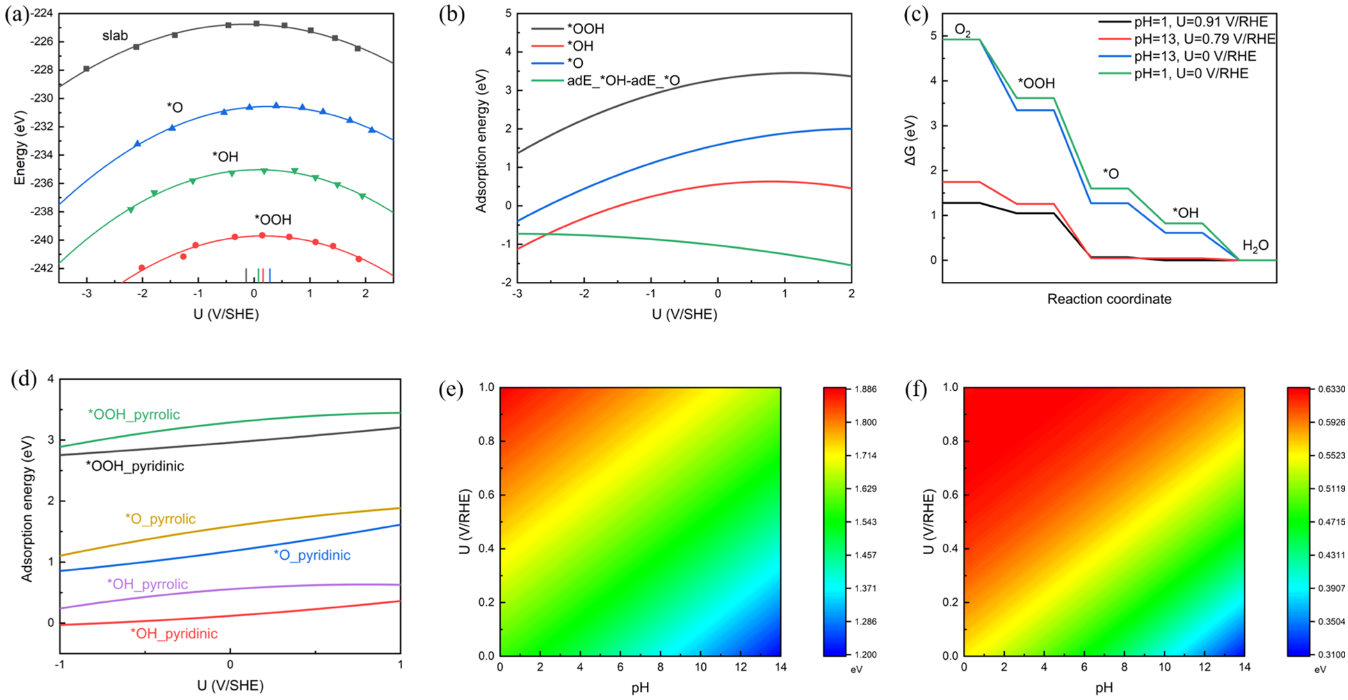

Figure 5. (a) Calculated energies of the bare pyrrolic FeN_4C slab (black) and corresponding three reaction intermediates (*OOH, red; *O, blue; *OH, green) as a function of the applied electrode potential. (b) Adsorption energies of *OOH, *O, and *OH and the difference between *OH and *O as a function of the applied electrode potential. (c) Free energy profile of ORR catalyzed by pyrrolic FeN_4C at U = 0.91 V/RHE, pH = 1; U = 0.79 V/RHE, pH = 13; U = 0 V/RHE, pH = 13; and U = 0 V/RHE, pH = 1. (d) Adsorption energies of *OOH, *O, and *OH as a function of the applied potential on pyridinic FeN_4C and pyrrolic FeN_4C. (e) pH-dependent and potential-dependent contour plot of adsorption energies of *O and (f) *OH on pyrrolic FeN_4C.

mechanism based on the constant-potential implicit model. The optimized atomic models of pyridinic FeN_4C and corresponding reaction intermediates (*OOH, *O, and *OH) at zero charge are shown in Figure 2. The calculated energies as a function of the applied electrode potential (referenced to the SHE scale) for pyridinic FeN_4C are shown in Figure 3a. All of the energy−potential points fit a quadratic relation nicely, and the detailed fitted parameters are shown in Table S2. Note that the calculated surface area normalized capacitance of pyridinic FeN_4C is 20.35 μF/cm, which is close to the experimental value, 21 μF/cm,[34] indicating the rationality and validity of our model. The adsorption energies of three reaction intermediates with respect to the applied potential are shown in Figure 3b. The adsorption energy of *O is significantly influenced by the applied potential, followed by *OOH and *OH. These different degrees of relevancy would affect the rate-determining step (RDS) and onset potential under different applied potentials and pH values, which will be discussed in detail below.

From the potential-dependent adsorption energies of reaction intermediates combined with the reaction mechanism, we obtained the pH-dependent free energy profile referenced to the RHE scale and corresponding onset potentials (under which the maximum free energy change is equal to 0). As shown in Figure 3c, the ORR onset potential at pH = 1 is determined to be 0.49 V vs RHE, which is larger than 0.32 V/RHE under pH = 13, and it demonstrates that the ORR catalyzed by pyridinic FeN_4C favors the acidic environment. The RDS is the *OH removal, indicating that the adsorption of *OH on pyridinic FeN_4C is too strong, and the RDS does not change along with pH. Figure 3d shows the pH-dependent and potential-dependent contour plots of adsorption energies of *OH on pyridinic FeN_4C. We could see that the adsorption strength of *OH on pyridinic FeN_4C increases as the pH increases or the applied potential decreases; thus, the alkaline environment would make the *OH removal even more difficult, which could explain the pH-dependent activity of pyridinic FeN_4C.

https://doi.org/10.1021/jacs.2c08743
J. Am. Chem. Soc. 2022, 144, 18144−18152

Recent experiments have reported that the pyrrolic-type FeN_4C is the origin of high ORR activity comparable to commercial 20% Pt/C,[8] and Li et al.[35] proposed a general strategy to prepare pyrrolic-N4-type SACs with Pt_1 catalysts. Nevertheless, only a few reports have studied pyrrolic FeN_4C as a model catalyst due to the relatively more complex model.[36] However, the limited local coordination information determined from the X-ray absorption fine structure and various types of N signals captured in XPS did not completely eliminate the possibility of pyrrolic-N-type FeN_xC as the active site.[37]

Due to the concerns above, we also evaluated the ORR mechanism catalyzed by pyrrolic FeN_4C. The optimized structures and corresponding ORR intermediates catalyzed by pyrrolic FeN_4C are shown in Figure 4. As shown in Figure 5a, the PZC of all intermediates and the pristine slab has positively shifted by about 0.7 V compared with Figure 3a. Moreover, the magnitude of the PZC shift compared with the pristine slab on pyrrolic FeN_4C is greater than that on pyridinic FeN_4C (Tables S2 and S3), indicating that the adsorption energies can change more rapidly as the applied potential varies, which is also confirmed in Figure 5b. The free energy profile on pyrrolic FeN_4C was also calculated to determine the ORR activity. As shown in Figure 5c, the onset potential is 0.91 and 0.79 V/RHE at pH = 1 and 13, respectively, showing substantially increased catalytic activity compared with pyridinic FeN_4C. Notably, the onset potential in acidic media is in good agreement with the experimental one, 0.90 V/RHE.[8] This activity promotion could be explained by the optimized adsorption strength as shown in Figure 5d. The adsorption strength of all three intermediates (*OOH, *O, and *OH) decreases compared with pyridinic FeN_4C. From the density of states (DOS) analysis shown in Figure S3, the DOS value around the Fermi level for pyrrolic FeN_4C is higher than that for pyridinic FeN_4C, indicating easier electron transfer from the catalyst to the adsorbate. Interestingly, we also found that the RDS changes from the *OH removal to the *O protonation step as the pH increases. We plotted the difference between the adsorption energies of *OH and *O in Figure 5b, and this difference slightly increases as the applied potential changes. So, according to the equation $U/\mathrm{RHE} = U/\mathrm{SHE} + k_BT\ln(10)\mathrm{pH}/e$, when U/RHE is fixed, different pH values lead to different U/SHE, which can explain the RDS change. In Figure 5e,f, over the onset potential range (from 0.79 to 0.91 V/RHE), the adsorption energy of *OH remains relatively constant as the pH varies; therefore, the RDS change is largely determined by the *O adsorption strength.

To further investigate how the number and type of coordinating N affect the ORR activity, we thoroughly calculated the ORR activity on other FeN_xC (x = 0−3) configurations with pyridinic- or pyrrolic-type N as shown in Figures 6 and S4−S14. Corresponding fitted parameters are shown in Tables S8−S18. The onset potential basically decreases as the number of coordinating N decreases for both pyridinic- and pyrrolic-type FeN_xC. Importantly, the computations of pyridinic-type FeN_xC are consistent with experiments.[33] Pyrrolic-type N-coordinated FeN_xC shows a higher activity than pyridinic-type N; therefore, we could improve the activity of FeN_xC by increasing the content of pyrrolic N in experiments via specific synthesis procedures and precursor design.[38] Notably, the RDS for these 13 different N-coordinated FeN_xC configurations is the *OH removal except for pyrrolic FeN_4C. We also evaluated the selectivity between

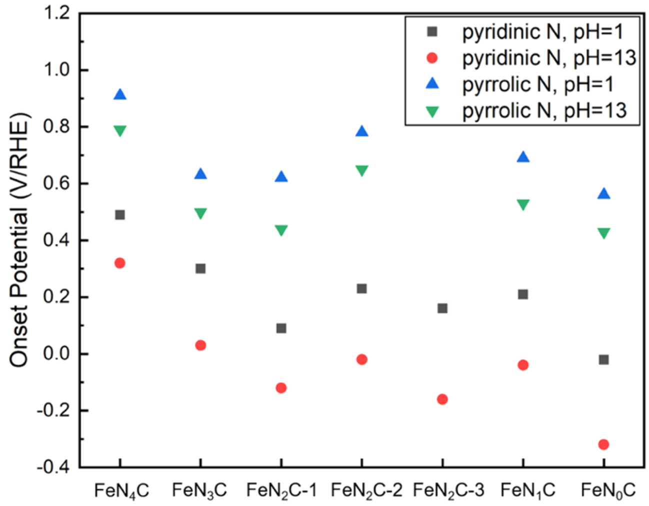

Figure 6. Onset potential (V/RHE) for the ORR catalyzed by 13 different N-coordinated FeN_xC configurations under pH = 1 and 13.

$2e^-$ and $4e^-$ ORR over these considered configurations, as shown in Figure S15; all of the considered configurations prefer $4e^-$ ORR. In the following discussion, we will focus on the FeN_4C case.

One of the major challenges faced by FeN_xC catalysts is their long-term stability due to the metal dissolution and subsequent highly oxidative hydroxyl formation, which will cause the carbon support corrosion due to the Fenton process and the deterioration of catalytic performance. Since *OH and *O bind the catalyst strongly, they could contribute to forming the new active site rather than poisoning the active site due to the two-dimensional nature of the catalyst.[39,40] However, due to the complexity of the catalytic system and intrinsic limitation of *in situ* characterization techniques, the nature of the axial ligand is still ambiguous. The transformation of active sites under working conditions is very interesting for study. At the same time, *in situ* ligand modification of the active site, like coadsorbed *O, *OH, or other types of axially adsorbing O_mH_n species have been identified to greatly affect the catalytic activity and reaction pathway in many reports.[41−44] As shown in Figure 7, here, we plot the stability diagram of pyridinic and pyrrolic FeN_4C based on the metal dissolution and water coadsorption caused by *in situ* ligand modification from a thermodynamic perspective. The details are shown in the Computational Methods part. The y is determined to be 2 and 3 for pyridinic and pyrrolic FeN_4C, respectively, by comparing the N protonation energy as described in Table S19. The stability is highly dependent on the N type and the local configuration of active sites, which was also reported previously.[27,45] As shown in Figure 7a,b, in acidic or neutral media, the most stable phase is dissolved Fe ion or $FeOH^{2+}$, which could explain the insufficient stability for PEMFC. However, under alkaline conditions at a relatively oxidative applied potential range, the most stable phase turns into an *O or *OH coadsorbed active site, indicating that *O or *OH could help stabilize the Fe site. As previously reported, pure or N-doped carbon materials showed certain ORR activity. We also evaluated the ORR mechanism catalyzed by pyridinic N_4H_2 and pyrrolic N_4H_3 as shown in Figures S16 and S17 to determine the effect on catalytic activity by metal dissolution. The onset potential for pyridinic N_4H_2 and pyrrolic N_4H_3 is

https://doi.org/10.1021/jacs.2c08743
J. Am. Chem. Soc. 2022, 144, 18144−18152

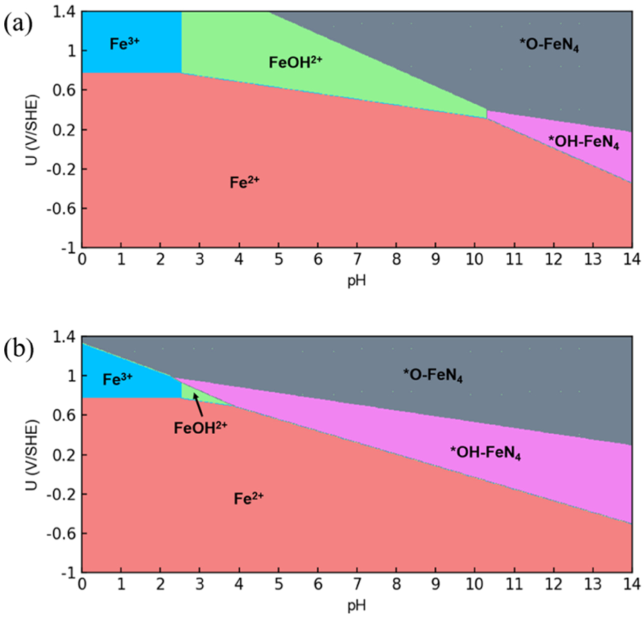

Figure 7. Stability diagram of the (a) pyridinic FeN_4C slab and (b) pyrrolic FeN_4C slab as a function of pH and applied potential.

0.18 and 0.20 V/RHE at pH = 1, respectively, which could explain the activity loss of FeN_4C in acidic media.

But what about the influence of the coadsorbed species on the ORR catalytic mechanism and the pH-dependent activity? Here, we also evaluated the ORR activity on pyridinic *O-FeN_4C and *OH-FeN_4C, as well as pyrrolic *O-FeN_4C and *OH-FeN_4C, based on the free energy profile as shown in Figure 8. The corresponding models and fitted parameters are shown in Figures S18−S21 and Tables S4−S7. The catalytic activity is remarkably promoted by the coadsorbed *O for pyridinic *O-FeN_4C in both acidic and alkaline media, with increasing the onset potential to 0.86 and 0.89 V/RHE under pH = 1 and 13, respectively. The RDS is the *OOH formation step, and the adsorption strength becomes stronger as the pH increases corresponding to the higher activity in the alkaline environment (Figure S22). As shown in Figure 8b, the coadsorbed *O would slightly decrease the activity of pyrrolic FeN_4C in both acidic and alkaline media. The RDS for pyrrolic *O-FeN_4C is also the *OOH formation step, which indicates the remarkable effect on *OOH bonding strength by coadsorbing *O. As shown in Figure 8c,d, interestingly pyridinic and pyrrolic *OH-FeN_4C show almost the same catalytic activity in both acidic and alkaline media. This leveling effect could be explained by the nearly identical adsorption energy of *OH (the intermediate within the RDS) of pyrrolic and pyridinic *OH-FeN_4C as shown in Figure S23. The coadsorbed *OH would increase the catalytic activity compared with pristine pyridinic FeN_4C, while the RDS remains to be the *OH removal. Nevertheless, the coadsorbed *OH would decrease the activity of pyrrolic FeN_4C.

On one hand, the axially coadsorbing species would contribute to stabilizing the Fe active site, which is conducive to its long-term stability. On the other hand, they also help

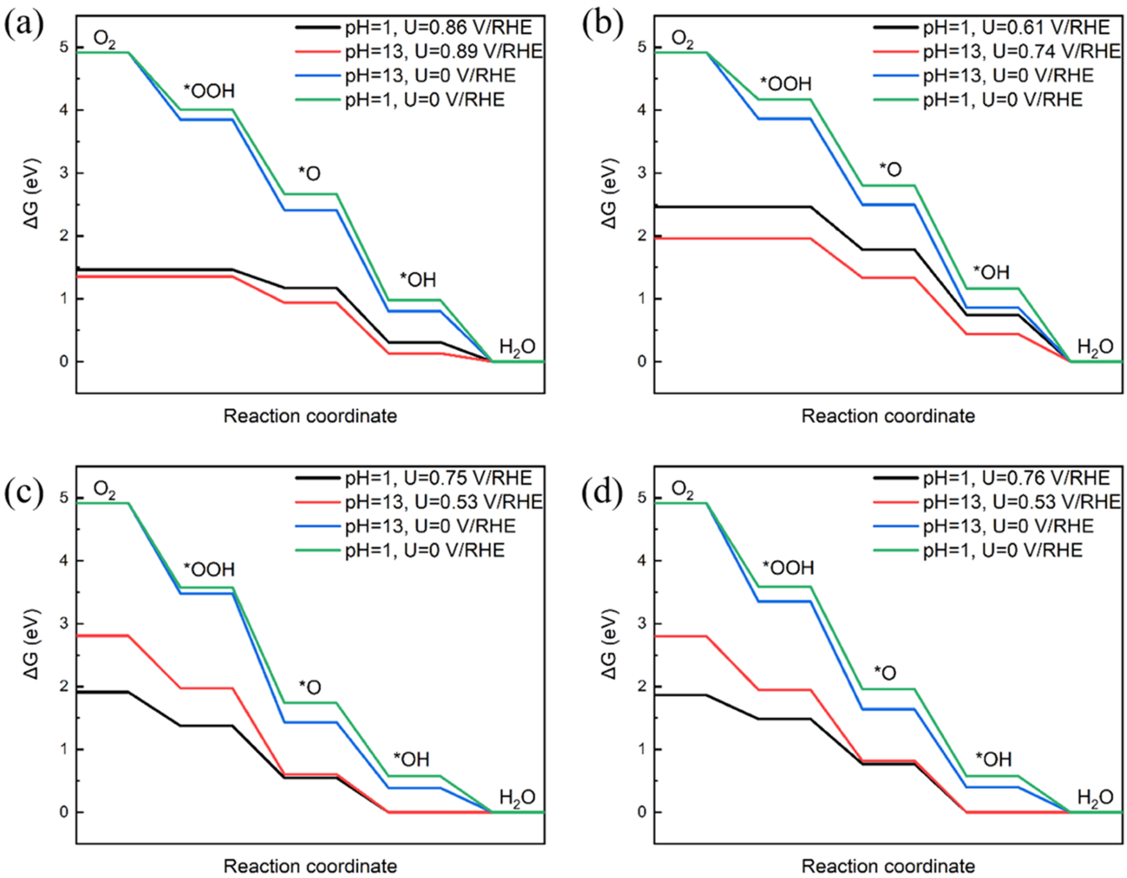

Figure 8. (a) Free energy profiles of ORR catalyzed by pyridinic *O-FeN_4C, (b) pyrrolic *O-FeN_4C, (c) pyridinic *OH-FeN_4C, and (d) pyrrolic *OH-FeN_4C.

https://doi.org/10.1021/jacs.2c08743
J. Am. Chem. Soc. 2022, 144, 18144−18152

alleviate the relatively strong adsorption strength of intermediates on pyridinic FeN_4C, thus leading to optimized adsorption energy and higher catalytic activity. The *in situ* transformation of catalytic active sites could explain why pyridinic FeN_xC catalysts exhibit better performance in alkaline media as reported in experiments.[13] However, the coadsorbing species would reduce the activity of pyrrolic FeN_4C.

Upon the acceptance of this work, we noticed the following papers published very lately. Hutchison et al.[46] demonstrated the effect of axial ligation on ORR by multilevel computations. Specifically, Ni et al.[47] found that the active site of Fe−N−C catalysts for ORR is the iron site coordinated with pyrrolic N by Mössbauer spectroscopy, which is consistent with our computations.

■ CONCLUSIONS

In conclusion, we comprehensively studied the ORR activity catalyzed by 13 different N-coordinated FeN_xC configurations through simulations based on the constant-potential implicit solvent model. Our results demonstrated that the pyrrolic FeN_xC shows superior catalytic activity to the pyridinic one, and among these, pyrrolic FeN_4C exhibits the highest activity in acidic media. The activity generally decreases as the number of coordinating N decreases for both pyridinic- and pyrrolic-type FeN_xC. Specifically, the *in situ* active site transformation to *O-FeN_4C in alkaline media for pyridinic FeN_4C explains the pH-dependent activity for broadly reported Fe−N−C catalysts, and these axially coadsorbing species can help stabilize the Fe site. Our results could provide valuable guidance for rational design of better durable Fe−N−C catalysts for ORR.

■ ASSOCIATED CONTENT

Supporting Information

The Supporting Information is available free of charge at https://pubs.acs.org/doi/10.1021/jacs.2c08743.

Optimized FeN_xC models and reaction models during ORR catalyzed by *O or *OH-FeN_4C; DOS analysis; calculated energies as a function of the applied potential and free energy profile; pH-dependent and potential-dependent contour plot of adsorption energy and difference of adsorption energies; tables of free energy of small molecules and fitted parameters of potential-dependent free energy; and details of Pourbaix diagram calculation (PDF)

■ AUTHOR INFORMATION

Corresponding Authors

Xu Zhang − *School of Chemical Engineering, Zhengzhou University, Zhengzhou 450001 Henan, China*; Email: zzuzhangxu@zzu.edu.cn

Zhen Zhou − *School of Materials Science and Engineering, Institute of New Energy Material Chemistry, Renewable Energy Conversion and Storage Center (ReCast), Key Laboratory of Advanced Energy Materials Chemistry (Ministry of Education), Nankai University, Tianjin 300350, China; School of Chemical Engineering, Zhengzhou University, Zhengzhou 450001 Henan, China*; orcid.org/0000-0003-3232-9903; Email: zhouzhen@nankai.edu.cn

Authors

Xu Hu − *School of Materials Science and Engineering, Institute of New Energy Material Chemistry, Renewable Energy Conversion and Storage Center (ReCast), Key Laboratory of Advanced Energy Materials Chemistry (Ministry of Education), Nankai University, Tianjin 300350, China*

Suya Chen − *School of Materials Science and Engineering, Institute of New Energy Material Chemistry, Renewable Energy Conversion and Storage Center (ReCast), Key Laboratory of Advanced Energy Materials Chemistry (Ministry of Education), Nankai University, Tianjin 300350, China*

Letian Chen − *School of Materials Science and Engineering, Institute of New Energy Material Chemistry, Renewable Energy Conversion and Storage Center (ReCast), Key Laboratory of Advanced Energy Materials Chemistry (Ministry of Education), Nankai University, Tianjin 300350, China*

Yun Tian − *School of Chemical Engineering, Zhengzhou University, Zhengzhou 450001 Henan, China*

Sai Yao − *School of Materials Science and Engineering, Institute of New Energy Material Chemistry, Renewable Energy Conversion and Storage Center (ReCast), Key Laboratory of Advanced Energy Materials Chemistry (Ministry of Education), Nankai University, Tianjin 300350, China*

Zhengyu Lu − *School of Materials Science and Engineering, Institute of New Energy Material Chemistry, Renewable Energy Conversion and Storage Center (ReCast), Key Laboratory of Advanced Energy Materials Chemistry (Ministry of Education), Nankai University, Tianjin 300350, China*

Complete contact information is available at: https://pubs.acs.org/10.1021/jacs.2c08743

Notes

The authors declare no competing financial interest.

■ ACKNOWLEDGMENTS

This work was supported by NSFC (21933006), and the computations were performed at the National Supercomputing Center in Zhengzhou, China.

■ REFERENCES

(1) Deng, Y.; Luo, J.; Chi, B.; Tang, H.; Li, J.; Qiao, X.; Shen, Y.; Yang, Y.; Jia, C.; Rao, P.; et al. Advanced Atomically Dispersed Metal−Nitrogen−Carbon Catalysts Toward Cathodic Oxygen Reduction in PEM Fuel Cells. *Adv. Energy Mater.* **2021**, *11*, No. 2101222.

(2) Kulkarni, A.; Siahrostami, S.; Patel, A.; Nørskov, J. K. Understanding Catalytic Activity Trends in the Oxygen Reduction Reaction. *Chem. Rev.* **2018**, *118*, 2302−2312.

(3) Zhao, C.-X.; Li, B.-Q.; Liu, J.-N.; Zhang, Q. Intrinsic Electrocatalytic Activity Regulation of M−N−C Single-Atom Catalysts for the Oxygen Reduction Reaction. *Angew. Chem., Int. Ed.* **2021**, *60*, 4448−4463.

(4) Zhang, X.; Chen, A.; Chen, L.; Zhou, Z. 2D Materials Bridging Experiments and Computations for Electro/Photocatalysis. *Adv. Energy Mater.* **2022**, *12*, No. 2003841.

(5) Xie, X.; Shang, L.; Xiong, X.; Shi, R.; Zhang, T. Fe Single-Atom Catalysts on MOF-5 Derived Carbon for Efficient Oxygen Reduction Reaction in Proton Exchange Membrane Fuel Cells. *Adv. Energy Mater.* **2022**, *12*, No. 2102688.

(6) Jiao, L.; Zhang, R.; Wan, G.; Yang, W.; Wan, X.; Zhou, H.; Shui, J.; Yu, S. H.; Jiang, H. L. Nanocasting SiO_2 into Metal-Organic Frameworks Imparts Dual Protection to High-loading Fe Single-Atom Electrocatalysts. *Nat. Commun.* **2020**, *11*, No. 2831.

(7) Zhang, N.; Zhou, T.; Chen, M.; Feng, H.; Yuan, R.; Zhong, Ca.; Yan, W.; Tian, Y.; Wu, X.; Chu, W.; et al. High-Purity Pyrrole-Type FeN_4 Sites as a Superior Oxygen Reduction Electrocatalyst. *Energy Environ. Sci.* **2020**, *13*, 111−118.

(8) Yang, L.; Cheng, D.; Xu, H.; Zeng, X.; Wan, X.; Shui, J.; Xiang, Z.; Cao, D. Unveiling the High-Activity Origin of Single-Atom Iron Catalysts for Oxygen Reduction Reaction. *Proc. Natl. Acad. Sci. U.S.A.* **2018**, *115*, 6626−6631.

(9) Zhang, Y.; Qian, L.; Zhao, W.; Li, X.; Huang, X.; Mai, X.; Wang, Z.; Shao, Q.; Yan, X.; Guo, Z. Highly Efficient Fe-N-C Nanoparticles Modified Porous Graphene Composites for Oxygen Reduction Reaction. *J. Electrochem. Soc.* **2018**, *165*, H510−H516.

(10) Wen, Y.; Ma, C.; Wei, Z.; Zhu, X.; Li, Z. FeNC/MXene Hybrid Nanosheet as an Efficient Electrocatalyst for Oxygen Reduction Reaction. *RSC. Adv.* **2019**, *9*, 13424−13430.

(11) Nørskov, J. K.; Bligaard, T.; Logadottir, A.; Kitchin, J. R.; Chen, J. G.; Pandelov, S.; Stimming, U. Trends in the Exchange Current for Hydrogen Evolution. *J. Electrochem. Soc.* **2005**, *152*, J23−J26.

(12) Nørskov, J. K.; Rossmeisl, J.; Logadottir, A.; Lindqvist, L.; Kitchin, J. R.; Bligaard, T.; Jónsson, H. Origin of the Overpotential for Oxygen Reduction at a Fuel-Cell Cathode. *J. Phys. Chem. B* **2004**, *108*, 17886−17892.

(13) Meng, H.; Jaouen, F.; Proietti, E.; Lefèvre, M.; Dodelet, J.-P. pH-Effect on Oxygen Reduction Activity of Fe-Based Electro-catalysts. *Electrochem. Commun.* **2009**, *11*, 1986−1989.

(14) Wan, K.; Yu, Z.-p.; Li, X.-h.; Liu, M.-y.; Yang, G.; Piao, J.-h.; Liang, Z.-x. pH Effect on Electrochemistry of Nitrogen-Doped Carbon Catalyst for Oxygen Reduction Reaction. *ACS Catal.* **2015**, *5*, 4325−4332.

(15) Zhang, X.; Zhou, Z. Perspective on Theoretical Models for CO_2 Electrochemical Reduction. *J. Phys. Chem. C* **2022**, *126*, 3820−3829.

(16) Hu, X.; Yao, S.; Chen, L.; Zhang, X.; Jiao, M.; Lu, Z.; Zhou, Z. Understanding the role of axial O in CO_2 electroreduction on NiN_4 single-atom catalysts via simulations in realistic electrochemical environment. *J. Mater. Chem. A* **2021**, *9*, 23515−23521.

(17) Filhol, J.-S.; Neurock, M. Elucidation of the Electrochemical Activation of Water over Pd by First Principles. *Angew. Chem., Int. Ed.* **2006**, *45*, 402−406.

(18) Taylor, C. D.; Wasileski, S. A.; Filhol, J.-S.; Neurock, M. First principles reaction modeling of the electrochemical interface: Consideration and calculation of a tunable surface potential from atomic and electronic structure. *Phys. Rev. B* **2006**, *73*, No. 165402.

(19) Duan, Z.; Henkelman, G. Theoretical Resolution of the Exceptional Oxygen Reduction Activity of Au(100) in Alkaline Media. *ACS Catal.* **2019**, *9*, 5567−5573.

(20) Kresse, G.; Furthmüller, J. Efficient Iterative Schemes for ab initio Total-energy Calculations Using a Plane-wave Basis Set. *Phys. Rev. B* **1996**, *54*, 11169−11186.

(21) Grimme, S.; Ehrlich, S.; Goerigk, L. Effect of the Damping Function in Dispersion Corrected Density Functional Theory. *J. Comput. Chem.* **2011**, *32*, 1456−1465.

(22) Monkhorst, H. J.; Pack, J. D. Special Points for Brillouin-Zone Integrations. *Phys. Rev. B* **1976**, *13*, 5188−5192.

(23) Yang, J.; Liu, W.; Xu, M.; Liu, X.; Qi, H.; Zhang, L.; Yang, X.; Niu, S.; Zhou, D.; Liu, Y.; et al. Dynamic Behavior of Single-Atom Catalysts in Electrocatalysis: Identification of Cu-N_3 as an Active Site for the Oxygen Reduction Reaction. *J. Am. Chem. Soc.* **2021**, *143*, 14530−14539.

(24) Mathew, K.; Kolluru, V. C.; Mula, S.; Steinmann, S. N.; Hennig, R. G. Implicit Self-Consistent Electrolyte Model in Plane-Wave Density-Functional Theory. *J. Chem. Phys.* **2019**, *151*, No. 234101.

(25) Mathew, K.; Sundararaman, R.; Letchworth-Weaver, K.; Arias, T. A.; Hennig, R. G. Implicit Solvation Model for Density-Functional Study of Nanocrystal Surfaces and Reaction Pathways. *J. Chem. Phys.* **2014**, *140*, No. 084106.

(26) Holby, E. F.; Wang, G.; Zelenay, P. Acid Stability and Demetalation of PGM-Free ORR Electrocatalyst Structures from Density Functional Theory: A Model for "Single-Atom Catalyst" Dissolution. *ACS Catal.* **2020**, *10*, 14527−14539.

(27) Patniboon, T.; Hansen, H. A. Acid-Stable and Active M−N−C Catalysts for the Oxygen Reduction Reaction: The Role of Local Structure. *ACS Catal.* **2021**, *11*, 13102−13118.

(28) Herranz, J.; Jaouen, F.; Lefèvre, M.; Kramm, U. I.; Proietti, E.; Dodelet, J.-P.; Bogdanoff, P.; Fiechter, S.; Abs-Wurmbach, I.; Bertrand, P.; et al. Unveiling N-Protonation and Anion-Binding Effects on Fe/N/C Catalysts for O_2 Reduction in Proton-Exchange-Membrane Fuel Cells. *J. Phys. Chem. C* **2011**, *115*, 16087−16097.

(29) Wang, Z.; Guo, X.; Montoya, J.; Nørskov, J. K. Predicting Aqueous Stability of Solid with Computed Pourbaix Diagram using SCAN Functional. *npj Comput. Mater.* **2020**, *6*, No. 160.

(30) Martinez, U.; Komini Babu, S.; Holby, E. F.; Chung, H. T.; Yin, X.; Zelenay, P. Progress in the Development of Fe-Based PGM-Free Electrocatalysts for the Oxygen Reduction Reaction. *Adv. Mater.* **2019**, *31*, No. 1806545.

(31) Meng, Y.; Li, K.; Yang, Y.; Wang, Y.; Wu, Z. The Oxygen Reduction Reaction Mechanism on FeN_3 Doped Divacancy Graphene: A Theoretical Perspective. *J. Electrochem. Soc.* **2018**, *165*, F145−F151.

(32) Shen, H.; Gracia-Espino, E.; Ma, J.; Tang, H.; Mamat, X.; Wagberg, T.; Hu, G.; Guo, S. Atomically FeN_2 Moieties Dispersed on Mesoporous Carbon: A New Atomic Catalyst For Efficient Oxygen Reduction Catalysis. *Nano Energy* **2017**, *35*, 9−16.

(33) Li, Y.; Liu, X.; Zheng, L.; Shang, J.; Wan, X.; Hu, R.; Guo, X.; Hong, S.; Shui, J. Preparation of Fe−N−C Catalysts with FeNx (x = 1, 3, 4) Active Sites and Comparison of Their Activities for the Oxygen Reduction Reaction and Performances in Proton Exchange Membrane Fuel Cells. *J. Mater. Chem. A* **2019**, *7*, 26147−26153.

(34) Chen, J.; Li, C.; Shi, G. Graphene Materials for Electrochemical Capacitors. *J. Phys. Chem. Lett.* **2013**, *4*, 1244−1253.

(35) Li, J.; Jiang, Y. F.; Wang, Q.; Xu, C. Q.; Wu, D.; Banis, M. N.; Adair, K. R.; Doyle-Davis, K.; Meira, D. M.; Finfrock, Y. Z.; et al. A General Strategy for Preparing Pyrrolic-N_4 Type Single-Atom Catalysts via Pre-located Isolated Atoms. *Nat. Commun.* **2021**, *12*, No. 6806.

(36) Wang, Y.; You, L.; Zhou, K. Origin of the N-Coordinated Single-Atom Ni sites in Heterogeneous Electrocatalysts for CO_2 Reduction Reaction. *Chem. Sci.* **2021**, *12*, 14065−14073.

(37) Wan, C.; Duan, X.; Huang, Y. Molecular Design of Single-Atom Catalysts for Oxygen Reduction Reaction. *Adv. Energy Mater.* **2020**, *10*, No. 1903815.

(38) Han, L.; Cheng, H.; Liu, W.; Li, H.; Ou, P.; Lin, R.; Wang, H.-T.; Pao, C.-W.; Head, A. R.; Wang, C.-H.; et al. A Single-Atom Library for Guided Monometallic and Concentration-Complex Multimetallic Designs. *Nat. Mater.* **2022**, *21*, 681−688.

(39) Jia, Q.; Ramaswamy, N.; Hafiz, H.; Tylus, U.; Strickland, K.; Wu, G.; Barbiellini, B.; Bansil, A.; Holby, E. F.; Zelenay, P.; Mukerjee, S. Experimental Observation of Redox-Induced Fe−N Switching Behavior as a Determinant Role for Oxygen Reduction Activity. *ACS Nano* **2015**, *9*, 12496−12505.

(40) Li, J.; Ghoshal, S.; Liang, W.; Sougrati, M.-T.; Jaouen, F.; Halevi, B.; McKinney, S.; McCool, G.; Ma, C.; Yuan, X.; et al. Structural and Mechanistic Basis for the High Activity of Fe−N−C Catalysts toward Oxygen Reduction. *Energy Environ. Sci.* **2016**, *9*, 2418−2432.

(41) Chen, K.; Liu, K.; An, P.; Li, H.; Lin, Y.; Hu, J.; Jia, C.; Fu, J.; Li, H.; Liu, H.; et al. Iron Phthalocyanine with Coordination Induced Electronic Localization to Boost Oxygen Reduction Reaction. *Nat. Commun.* **2020**, *11*, No. 4173.

(42) Rebarchik, M.; Bhandari, S.; Kropp, T.; Mavrikakis, M. How Noninnocent Spectator Species Improve the Oxygen Reduction Activity of Single-Atom Catalysts: Microkinetic Models from First-Principles Calculations. *ACS Catal.* **2020**, *10*, 9129−9135.

https://doi.org/10.1021/jacs.2c08743
J. Am. Chem. Soc. 2022, 144, 18144−18152

(43) Wang, Y.; Tang, Y. J.; Zhou, K. Self-Adjusting Activity Induced by Intrinsic Reaction Intermediate in Fe−N−C Single-Atom Catalysts. *J. Am. Chem. Soc.* **2019**, *141*, 14115−14119.
(44) Yang, X.; Xia, D.; Kang, Y.; Du, H.; Kang, F.; Gan, L.; Li, J. Unveiling the Axial Hydroxyl Ligand on Fe-N_4-C Electrocatalysts and Its Impact on the pH-Dependent Oxygen Reduction Activities and Poisoning Kinetics. *Adv. Sci.* **2020**, *7*, No. 2000176.
(45) Li, J.; Sougrati, M. T.; Zitolo, A.; Ablett, J. M.; Oğuz, I. C.; Mineva, T.; Matanovic, I.; Atanassov, P.; Huang, Y.; Zenyuk, I.; et al. Identification of Durable and Non-Durable FeN_x Sites in Fe−N−C Materials for Proton Exchange Membrane Fuel Cells. *Nat. Catal.* **2021**, *4*, 10−19.
(46) Hutchison, P.; Rice, P. S.; Warburton, R. E.; Raugei, S.; Hammes-Schiffer, S. Multilevel Computational Studies Reveal the Importance of Axial Ligand for Oxygen Reduction Reaction on Fe−N−C Materials. *J. Am. Chem. Soc.* **2022**, *144*, 16524−16534.
(47) Ni, L.; Gallenkamp, C.; Wagner, S.; Bill, E.; Krewald, V.; Kramm, U. I. Identification of the Catalytically Dominant Iron Environment in Iron- and Nitrogen-Doped Carbon Catalysts for the Oxygen Reduction Reaction. *J. Am. Chem. Soc.* **2022**, *144*, 16827−16840.

https://doi.org/10.1021/jacs.2c08743
J. Am. Chem. Soc. 2022, 144, 18144−18152